Primljen / Received: 23.1.2021.
Ispravljen / Corrected: 10.5.2020.
Prihvaćen / Accepted: 24.6.2020.
Dostupno online / Available online: 10.10.2025.

Research on the seismic performance of frame structures with external fractal dimension-buckling restrained braces

Authors:



Yubo Ren, MSc. CE 2483558012@qq.com



Xiaobo Luo, PhD. CE lutlxb123@163.com Corresponding author



Luchao Ma, MSc. CE 2918001838@qq.com

Qinghai University, China Faculty of Civil Engineering Key Laboratory of Energy-saving Building Materials and Engineering Safety of Qinghai, China

Yubo Ren, Xiaobo Luo, Luchao Ma

Research Paper

Research on the seismic performance of frame structures with external fractal dimension-buckling restrained braces

This study aimed to mitigate seismically induced displacement and deformation in reinforced concrete frame structures, thereby reducing earthquake-related damage and enhancing their structural seismic resilience. A novel fractal dimension-buckling restrained brace (FD-BRB), designed using MATLAB and Mandelbrot-derived fractal geometry, was applied for external frame retrofitting, and its seismic performance enhancement was quantified through ABAQUS simulations by comparing the structural behaviour before and after strengthening. This results demonstrate that externally applied FD-BRBs effectively mitigate localised damage in reinforced concrete frame structures under seismic loading, thereby reducing deformation and torsion. This intervention enhances the seismic performance and load capacity, extends the service life, lowers maintenance costs, and provides an efficient structural retrofitting solution that advances innovation in seismic-resistant systems.

Key words:

reinforced concrete frame structure, fractal dimension, buckling restrained brace, seismic performance, external reinforcement

Prethodno priopćenje

Yubo Ren, Xiaobo Luo, Luchao Ma

Istraživanje potresnog ponašanja okvirnih konstrukcija s vanjskim vezovima fraktalne dimenzije sa spriječenim izvijanjem

Cilj ovog istraživanja bio je smanjiti pomake i deformacije izazvane potresom u armiranobetonskim okvirnim konstrukcijama kako bi se umanjila oštećenja uslijed potresa i povećala njihova potresna otpornost. Za potrebe vanjskog ojačanja okvirnih konstrukcija primijenjen je novi vez fraktalne dimenzije sa spriječenim izvijanjem (engl. fractal dimension – buckling restrained brace, FD-BRB), razvijen u MATLAB-u na temelju fraktalne geometrije inspirirane Mandelbrotovim skupom. Učinak poboljšanja ponašanja u potresu ocijenjen je simulacijama u ABAQUS-u, usporedbom ponašanja konstrukcije prije ojačanja i nakon njega. Dobiveni rezultati pokazuju da vanjski FD-BRB vezovi učinkovito ublažavaju lokalna oštećenja u armiranobetonskim okvirnim konstrukcijama pri djelovanju potresnog opterećenja, čime se smanjuju deformacije i torzija. Takva intervencija poboljšava potresno ponašanje i nosivost konstrukcije, produljuje vijek trajanja, smanjuje troškove održavanja te predstavlja učinkovito rješenje za konstrukcijsku sanaciju koje doprinosi razvoju inovativnih sustava otpornih na potres.

Ključne riječi:

armiranobetonska okvirna konstrukcija, fraktalna dimenzija, vez sa spriječenim izvijanjem dijagonala, potresna svojstva, vanjsko ojačanje

1. Introduction

Given the increasing frequency of seismic events and the inadequate seismic performance of existing structures, seismic retrofitting has emerged as a crucial strategy for mitigating earthquake risks and ensuring structural safety. In general, retrofitting methods for existing structures can be categorised into structural- and component-level strengthening methods. Currently, the use of bucklingrestrained braces (BRBs) for the structural-level retrofitting of existing buildings has been widely studied and applied. Sarno et al. [1] conducted quasi-static tests on full-scale reinforced concrete (RC) frames and confirmed that BRB introduction enhanced the energy dissipation capacity of the structure by more than 60 %, significantly improving the ductility and energy-dissipation mechanisms of the frame system. Hamdy et al. [2] applied single-diagonal BRBs to retrofit a six-story RC building, increasing the base shear capacity by 150 %, thereby verifying the applicability of BRBs in high-rise buildings. Mirtaheri et al. [3, 4] performed response history analyses (RHAs) on two-dimensional (2D) frame systems with BRBs of varying lengths at different heights and proposed a formula for calculating the optimal steel core length of BRBs. Bai et al. [5] proposed a RC BRB frame that considered post-yield mechanisms and developed a dual-system seismic design procedure for different BRB configurations (including single-, V-, and inverted V-shapes), enabling collaborative energy dissipation between the BRBs and RC frames. Li et al. [6] conducted cyclic loading tests on a two-story, three-span RC frame equipped with K-shaped BRBs and found that the structural load-bearing capacity increased by 80 % and the energy-dissipation capacity improved by 50 %, providing design recommendations for enhancing the ductility and energy dissipation of RC frames. Khelfi et al. [7] quantified masonry infill contributions to RC frames using an equivalent diagonal strut model and the indices of performance (IP) method, demonstrating that tapered beam-column connections increase the infill strength participation by 86.2 %, significantly enhancing the energy-dissipation synergy. Valarmathi et al. [8] improved frame materials with basalt fibre-reinforced concrete (BFRC), where a fibre content of 0.25 % increased the cumulative energy dissipation by 28.2 % while reducing crack widths. Koman et al. [9] developed mortarless blocks with polymerflexible joints, achieving a 17 % greater load capacity than conventional infills while maintaining a near-bareframe initial stiffness and 86-mm ultimate displacement, preventing out-of-plane failures. Kallioras et al. [10] employed textile-reinforced mortar (TRM) integrated with thermal insulation to simultaneously enhance the seismic resistance and energy efficiency of RC structures. Full-scale seismic tests demonstrated minimal structural damage at a peak ground acceleration of 0.40 g, while air infiltration rates were reduced by 69 % to 78 %.

Despite these significant advancements, the aforementioned studies focused on internal retrofitting techniques that require intrusion into a building's interior space during construction and may affect existing functions. Additionally, direct BRB connection may lead to concentrated damage in weak RC beam-column joints [11-16]. By contrast, external strengthening techniques can mitigate these issues [17-20]. Bergami [21] pioneered this approach through an Additional Dissipative Structure (ADS), utilising a freestanding external energy-dissipating tower to redirect seismic forces to new foundations via a displacement-oriented iterative design. This system demonstrated a 28 % reduction in the original foundation shear while eliminating internal disturbances. Olivo et al. [22] implemented a genetic algorithm optimisation for steel exoskeletons, synergistically determining the component quantity, spatial configuration, and sizing to minimise steel usage. The design incorporated story-drift limits (h/600) and EC3-compliant strength verification, achieving 40 to 60 % base shear transfer and up to 65 % more uniform story-drift reduction. However, most existing external braces adopt single geometric forms whose abrupt stiffness transitions can easily cause localised damage concentration.

Accordingly, this paper proposes an externally placed fractal dimension buckling-restrained brace (FD-BRB) for the overall retrofitting of reinforced concrete frame (RCF) structures [23]. By introducing a multi-level self-similar branching structure based on fractal geometry, two major breakthroughs were achieved in this study. First, the fractal structure dissipates seismic energy through the progressive yielding of secondary branches, effectively avoiding local failures commonly found in conventional external braces and significantly enhancing the overall seismic performance of the structure. Second, the multi-scale characteristics of the fractal structure allow flexible adaptation to the stiffness distribution of the original structure. Through multi-scale deformation regulation, story drift is more uniformly distributed, thereby reducing local abrupt variations and improving the overall stability and safety of the structure.

2. Numerical simulation of the substructure

The authors of this paper previously conducted experimental studies on a one-bay, three-story, two-span steel-frame structure, demonstrating significant reinforcement effectiveness [24–26]. Based on these findings, a two-story, four-column RCF structure was designed to evaluate the external reinforcement performance. The key metrics, including story drift, concrete damage evolution, steel stress distribution, and energy-dissipation capacity, were evaluated before and after retrofitting. This scaled configuration was selected by considering the solid modelling complexity, testing periodicity, and site constraints. The geometry of the structure is illustrated in Figure 1, and the detailed dimensions are provided in Section 3.2.



Figure 1. Geometry of the RCF structure investigated in this study

2.1. Constitutive models for steel and concrete

According to the Code for Design of Concrete Structures [27], a concrete damaged plasticity (CDP) model was used for solid modelling (Figure 2). The symbols in Figure 2 are as follows:

 $\sigma_{t0} = -$ maximum tensile stress in the elastic range $\varepsilon_{0t}^{el} \varepsilon_{t}^{el} = -$ elastic tensile strain without and with damage

 $\tilde{\varepsilon}_t^{pl}$, $\tilde{\varepsilon}_t^{ck}$ – plastic and inelastic tensile strains

 $\sigma_{\rm co'} \, \sigma_{\rm cu} \, - {\rm maximum} \, {\rm compressive} \, {\rm stresses} \, {\rm in} \, {\rm the} \, {\rm elastic} \, {\rm range} \, \,$ and concrete

 ε_{0c}^{el} , ε_{c}^{el} — elastic compressive strain without and with damage $\widetilde{\varepsilon}_{c}^{pl}$, $\widetilde{\varepsilon}_{c}^{in}$ — plastic and inelastic compressive strains.

For steel, a bilinear kinematic hardening model accounting for the Bauschinger effect was adopted (Figure 3). To approximate real engineering conditions as closely as possible, a defect ratio factor of 0.4‰ of the core unit length

was applied as the initial defect for the simulations. The friction coefficient was set to 0.1, and a 1/2 scaled model of the frame was used.

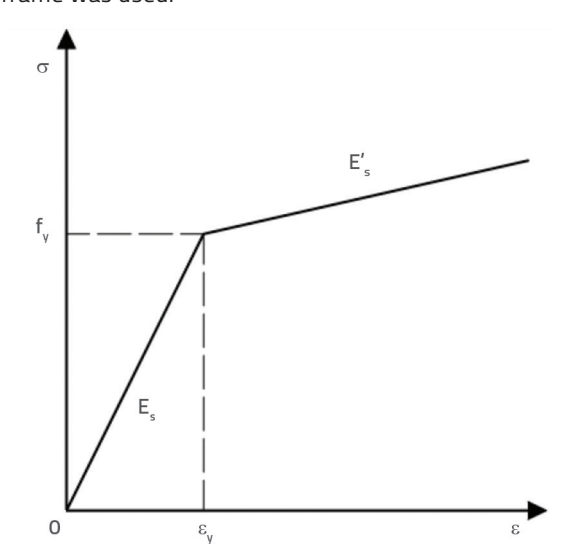
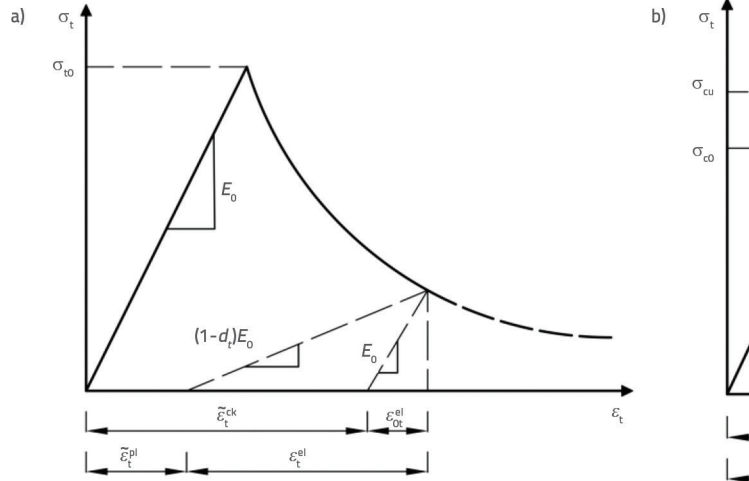


Figure 3. Stress-strain relationship of steel

2.2. Lateral stiffness ratio

In a concrete frame structure system with FD-BRBs, the horizontal forces are shared by the frame and braces, indicating that the lateral resistance can be obtained by the superposition illustrated in Figure 4.a [28, 29].

Previous studies [24] have confirmed that conventional bracing systems offer limited horizontal force sharing with frames. During the elastic stage, such braces provide supplemental lateral stiffness; however, the inelastic stage exhibits minimal force redistribution, leaving frames to resist most seismic demands. Conversely, the FD-BRB system fundamentally modifies the load-transfer pathways. It enhances the lateral stiffness in the elastic stage, while progressively assuming significant force-sharing responsibility in the inelastic stage.



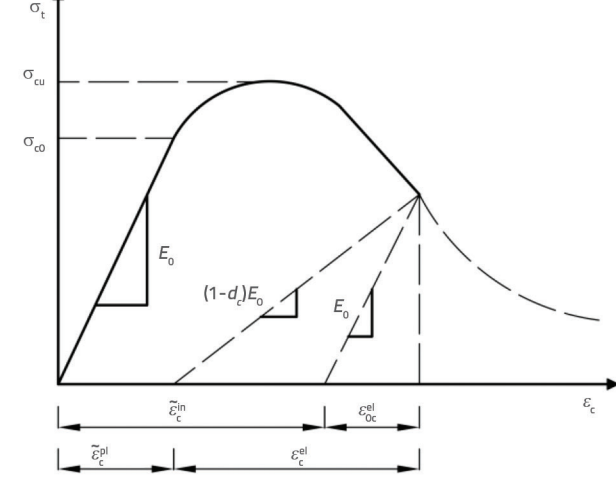
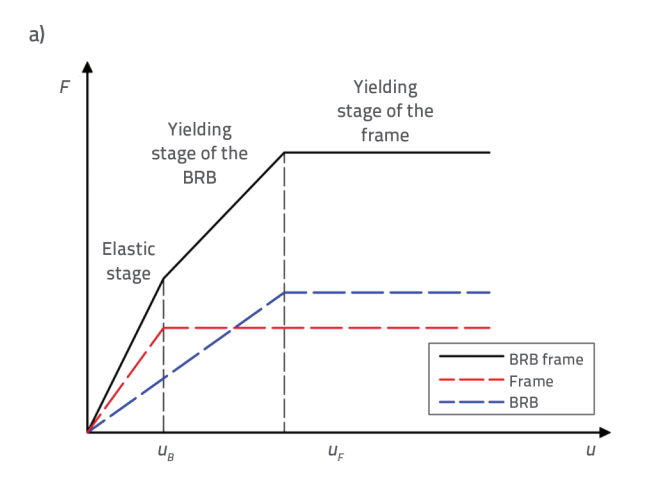


Figure 2 Stress-strain relationships of concrete: a) Tensile state; b) Compression state



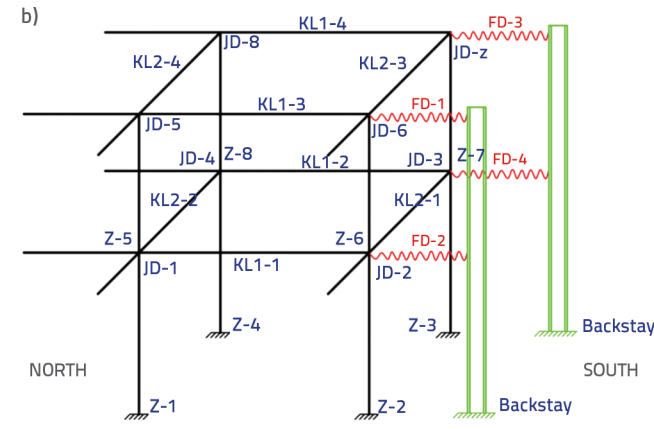


Figure 4. Structural system of the BRB frame: a) Mechanical model; b) Component composition and numbering; the symbols: *F* - horizontal force, *u* - horizontal displacement, *u*_s - yield displacement of the FD-BRBs, *u*_c - yield displacement of the frame structures

This behaviour protects the primary frames and validates the model's applicability.

From Figure 4.a, it can be observed that the mechanical model of a frame structure with BRBs under a lateral force can be simplified into a trilinear model. As the lateral force increases, the structural system transitions sequentially through three stages: the elastic stage of the BRBs and frame structure, the yielding stage of the BRBs with the frame structure remaining elastic, and the yielding stage of the overall structural system. As the horizontal seismic force increases further, plastic deformation continues to develop, the lateral stiffness of the structure gradually decreases, and the different components yield sequentially. The braces are designed to yield before the main frame structure, which requires the lateral stiffness of the BRBs to be controlled within a specific range during the preliminary design. Therefore, the rational allocation of lateral stiffness between the braces and frame structure is crucial for minimising the seismic response of the retrofitted system. The components of the retrofitted system used in the experimental simulations are illustrated in Figure 4.b.

The appropriate range for the lateral stiffness ratio k of the FD-BRBs within the retrofitted frame was calculated as follows:

$$k = k_o/k_f \tag{1}$$

where k_d and k_f are the lateral stiffnesses of the FD-BRBs and frame structure, respectively.

In the frame structure, the lateral stiffness of each story can be determined using the D-value method, as follows:

$$D = \sum_{i=1}^{n} \alpha \frac{12k_c}{h^2} \tag{2}$$

where D is the lateral stiffness of the floor; α is the coefficient of influence of the frame node rotation on the lateral stiffness of the column; n is the number of columns per floor; k_c is the linear stiffness of the column; and h is the story height.

After determining the lateral stiffness of each story in the frame, the *k* was set to 0.0, 0.5, 1.0, 1.5, 2.0, 2.5, 3.0, 3.5, and 4.0. Using the lateral stiffness ratio formula in Eq. (1), the corresponding stiffness of the BRB was calculated. Subsequently, by applying the horizontal–lateral stiffness formula for the BRB in Eq. (3), the equivalent cross–sectional area of the BRB was determined. Finally, specimens with calculated dimensions were fabricated to perform external retrofitting on the frame structure. This process ensures that the BRBs provide the desired lateral stiffness contribution, improving the overall seismic performance of the retrofitted frame.

$$k_{d} = 2E_{a}A_{c}\cos^{2}\theta/L \tag{3}$$

where E_e is the equivalent modulus of elasticity; A_e is the brace equivalent cross-sectional area; θ is the angle of the brace to the horizontal plane; and L is the total length of the brace.

3. Experimental framework for the pre-retrofit low-cyclic loading simulation analysis

3.1. Model establishment

During the model element selection, the BRBs were assumed to bear axial forces under low cyclic loading, whereas the frame structure and backstay were subjected to compression-bending forces. To analyse the stress conditions of the externally retrofitted FD-BRB frame structure, the following elements were selected:

- C3D8R elements for the concrete structures, BRBs, and H-shaped steel.
- T3D2 elements for the reinforcement bars.

The loading conditions include the following:

- A vertical load of 660 kN was applied to the top beam.
- Uniformly distributed loads of 37 kN were applied to the first and second floors.

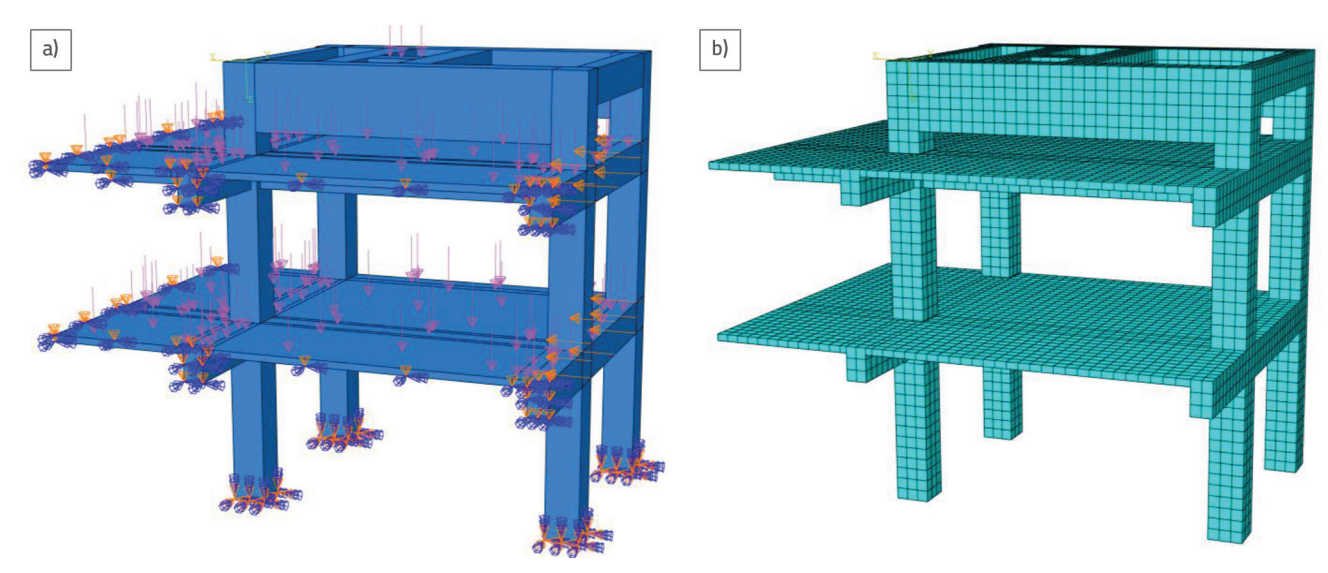


Figure 5. Modelling process of the test frame before retrofitting: a) Constraints and applied loads; b) Meshing

- Fixed constraints were applied to the base of all four columns.
- ZSYMM boundary conditions (U3 = UR1 = UR2 = 0) were applied to the incomplete beam-slab boundaries.

For mesh discretisation, different mesh sizes were assigned based on the dimensions of the structural components, as follows: beams and columns: 100 mm and slabs: 30 mm. The primary modelling process is illustrated in Figure 5. The softening behaviour of concrete was simulated using the CDP model, and a mesh sensitivity analysis was required to address the effect of finite element meshes on the results. By creating meshes with different densities and observing the trends of the key results, including the peak load, principal stress, and critical displacement, a mesh with relatively stable results was obtained, thus ensuring the accuracy of the simulation results. The loading system is shown in Figure 6.

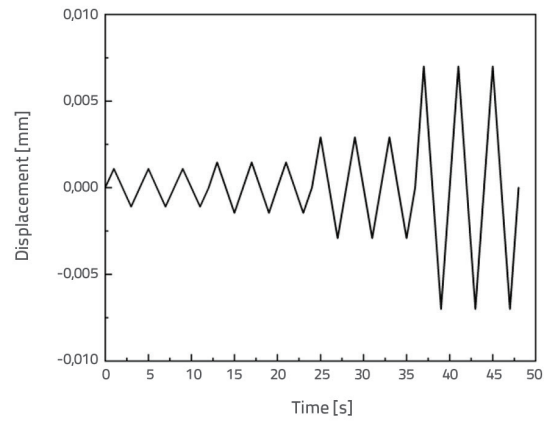


Figure 6. Loading system

3.2. Reinforcement stress and displacement

In this study, the longitudinal reinforcement was tertiary and the hoop reinforcement was the primary reinforcement. The size of the column network (Figure 7.a) was 2000×3000 mm, 90 mm east of the axial distance, and 90 mm south of the axial distance. The column cross-sectional size was 300×300 mm, with reinforcement of 4012 and hoop reinforcement of 4012 and distance 75 to 150 mm.

The cross-sectional size (Figures 7.b and 7.c) of the first and first floor beams was 180 × 300 mm, the upper and lower reinforcements were 2Ø12, and the hoop reinforcement was Ø6at a distance 75 to 150 mm; the cross-sectional size of the top floor beams was 300 × 600 mm, the upper compression reinforcement was 2020, the lower tensile reinforcement was 5020, and the hoop reinforcement was 06at a distance 75 to 150 mm. The plate thickness was 60 mm, the plate reinforcement was Ø6 at a distance 120 mm, and the plate configuration was bidirectional. The height of the ground floor was 1680 mm, that of the second floor was 1500 mm, and the top floor was a load floor without a floor slab with a height of 800 mm. The left cantilever of the lateral elevation exceeded the axis by 1000 mm, the left cantilever of the forward elevation exceeded the axis by 1200 mm, and the hoop reinforcement was Ø6at a distance 75 to 150 mm.

The stress and displacement distributions of the reinforcement in the pre-retrofit frame structure were analysed (Figure 8). The stress cloud diagram (Figure 8.a) reveals significant stress concentrations at column bases and beam-column joints under low-cycle loading. Moderate stress concentrations occur in the bottom slab, while other regions exhibit comparatively low stress levels. This distribution identifies column foundations and connections as critical seismic vulnerability zones, most susceptible to cyclic damage.

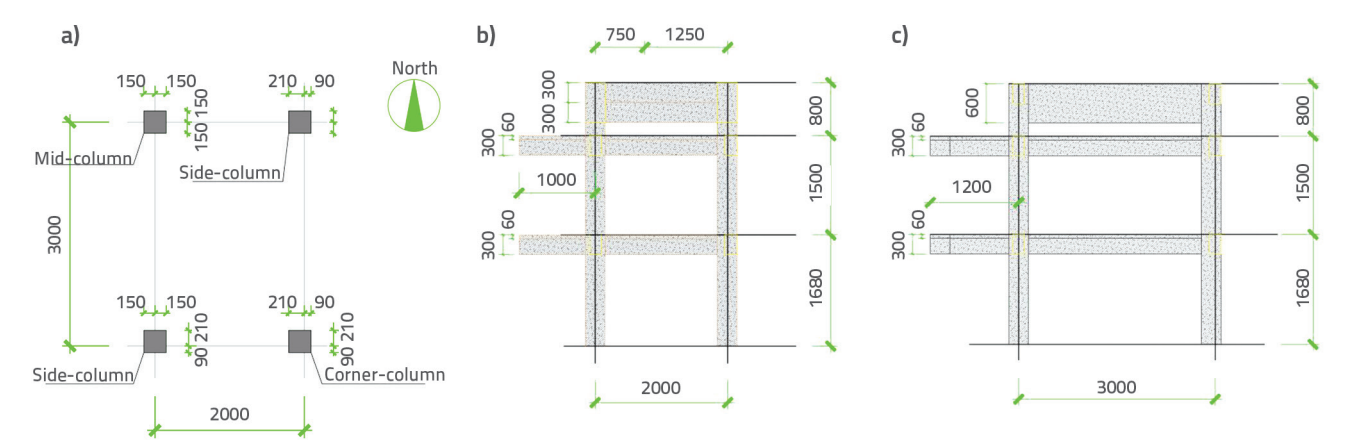


Figure 7. Model schematics: a) Column network; b) Side elevation; c) Front elevation

The displacement cloud diagram (Figure 8.b) indicates that the peak deformation occurs at the top loading beam. However, the maximum displacement (16.8 mm) is localized near the second-floor beam-column joints and adjacent slabs in the

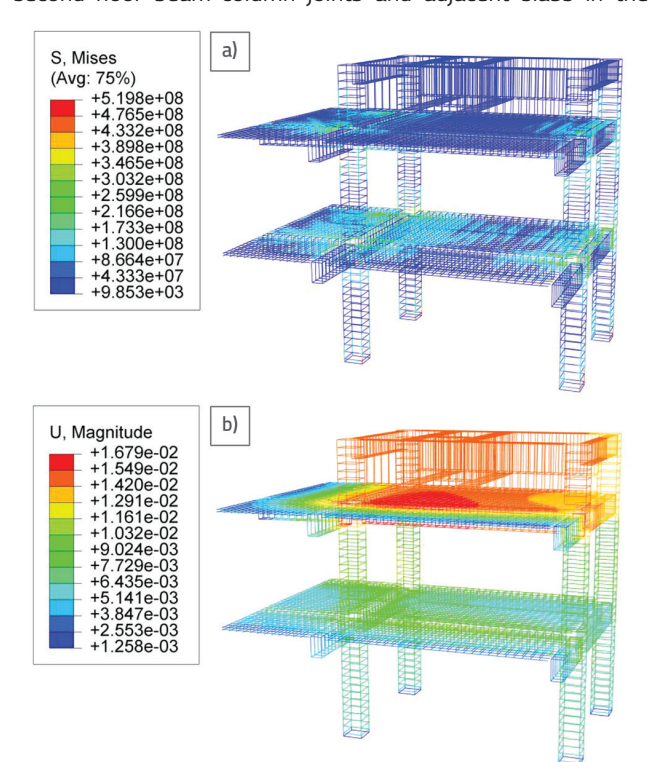


Figure 8. Reinforcement cloud diagrams of the frame before retrofitting: a) Stress; b) Displacement

mid-column region, resulting from upper-level vertical loading eccentricity. Substantial displacements also develop in the second-floor beams near the horizontal load application points. Conversely, minimal displacement occurs in the peripheral slabs and columns. The column bases exhibit negligible displacement due to constraints.

Figure 9 shows the stress and displacement distributions in several first-floor frame structures.

For mid-column Z-1 (Figure 9.a), stress concentrations occur at the upper joint, column base, and KL1-1 beam midspan. The maximum bearing capacity is 45.9 kN in these regions. The joint displacement (Figure 9.b) remains minimal owing to the constraints at the column base. The maximum displacement (0.012 mm) occurs at the KL1-1 midspan.

For corner column Z-3 (Figure 9.c), the maximum stress is localised at the column base, and the secondary stress concentrations are localised at the joint and midspan of the beam. Beam KL1-2 (Figure 9.d) exhibits the maximum displacement (0.014 mm) at the midspan bottom.

Similarly, Figure 10 shows the responses of various selected second-floor components. Significant stress concentrations occur at the Z-5 joint and KL1-3 beam midspan (Figure 10.a), with KL2-4 exhibiting substantially lower stresses. Pronounced displacement occurs at joint Z-5, adjacent beams, and cantilevered ends of KL1-3 and KL2-4 (Figure 10.b). This response indicates complex multi-directional loading at Z-5, which induces structural torsion in this column. This torsional behaviour results from the combined vertical eccentricity and horizontal forces.

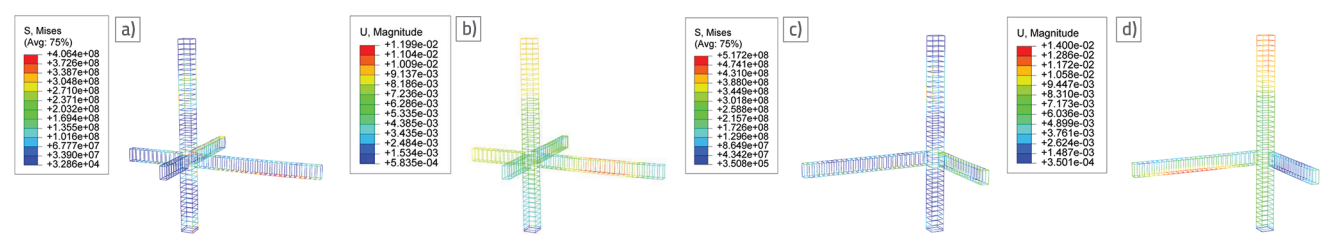


Figure 9. Reinforcement cloud diagrams of the first-floor beams, columns, and joints: a) Z-1 and associated component stresses; b) Z-1 and associated component displacements; c) Z-3 and associated component stresses; d) Z-3 and associated component displacements

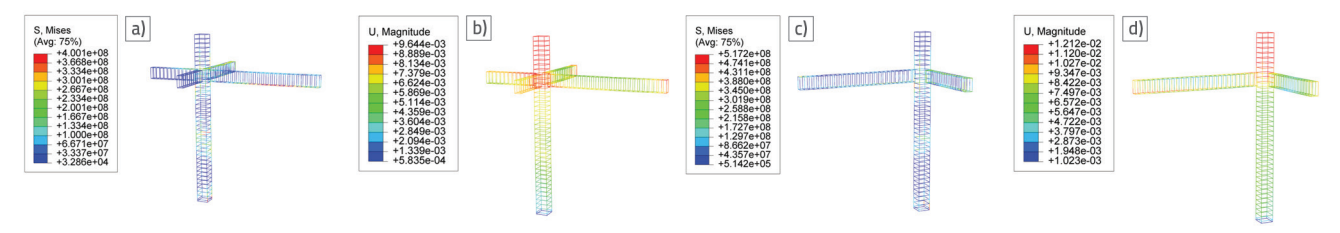


Figure 10. Reinforcement cloud diagrams of the second-floor beams, columns, and joints: a) Z-5 and associated component stresses; b) Z-5 and associated component displacements; c) Z-7 and associated component stresses; d) Z-7 and associated component displacements

For corner column Z-7 (Figure 10.c), the maximum stress is localised at the joint and the lower part of the column connected to it, followed by the stress at KL1-4 and its corresponding joint. However, the column and KL2-3 are relatively small, confirming that the joints are critical load-transfer regions. The maximum displacement occurs at the corner-column joint and the upper part of the connected column (Figure 10.d), followed by the lower tensile region of KL1-4. Minimal displacement occurs at KL2-3 and the column. However, compared with the middle column in Figure 10b, the stress and displacement of the corner column are higher, and the loading conditions are more complex. The displacement at the column base remains minimal due to constraints.

3.3. Equivalent plastic strain and displacement of concrete

The equivalent plastic strain and displacement cloud diagrams of concrete in the pre-retrofitted frame structure are shown in Figure 11. Significant concrete damage (Figure 11.a) is observed at the joints of the frame structure, and the damage on the first floor is greater than that on the second floor. Additionally, plastic damage to the columns of both floors is generally minor, and the damage to the beams and slabs is relatively small. Among the beams, KL1-1-KL1-4 on the first floor exhibit more damage than KL2-1-KL2-4 on the second floor. The displacement cloud diagram (Figure 11.b) indicates that the displacement patterns of the first and second floors are consistent with the changes observed in Figure 8.b. The maximum displacement (17.2 mm) occurs near the middle

and concrete work in coordination, thereby validating the feasibility of the simulated interaction between the two materials.

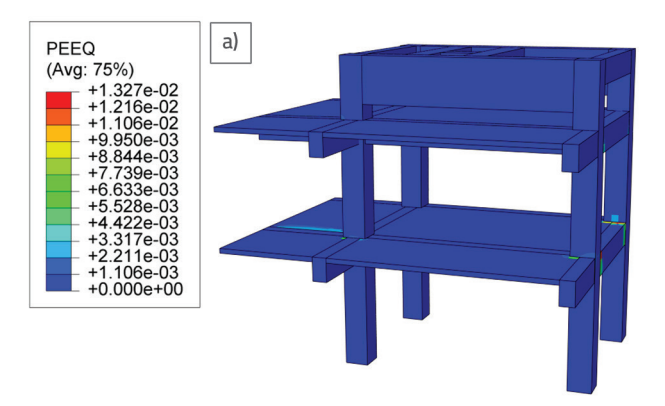
column of the second floor, indicating that the reinforcement

4. Experimental framework for the post-retrofit low-cyclic loading simulation analysis

4.1. Model establishment

Four FD-BRB components were added to the pre-retrofit structure (Figure 12) and connected to the backstays to form a composite retrofitting system. Through the parametric analysis described in Section 2.2, the stiffness ratio from 0.0 to 4.0 was examined, revealing that this parameter significantly governs shear distribution between the BRBs and the frame. To achieve optimal energy-dissipation synergy, the shear ratio must be maintained within a specific range [30]. A comparative analysis identified k=4 as the optimal configuration, yielding a stable shear ratio of 0.8. This condition simultaneously maximises the BRB energy-dissipation capacity and prevents load-bearing degradation in the frame members; thus, it was finally selected for the reinforcement design. The contact conditions were as follows:

- The "Hard contact" condition with frictionless tangential behaviour was specified between the core element and external constraint elements of the BRBs.
- The connecting segments at both ends of the BRBs were tied to the beam-column joints of the frame and the flange of the backstay using the tie constraint.



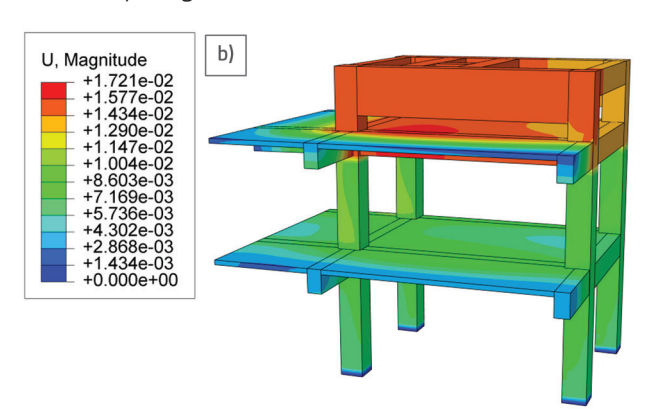


Figure 11. Concrete cloud diagrams of the frame before retrofitting: a) Equivalent plastic strain; b) Displacement

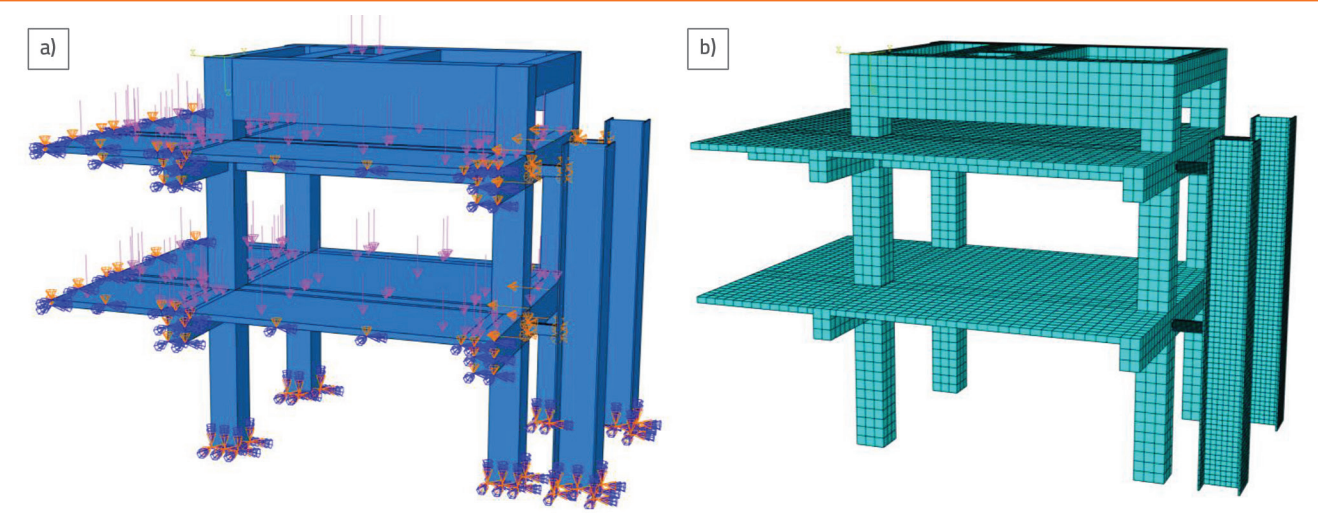


Figure 12. Modelling process for the test frame after retrofitting: a) Constraints and applied loads; b) Meshing

The boundary and loading conditions were specified as in the pre-retrofit model, with the constraint (UX = UY = UZ = URX = URY = URZ = 0) applied to the backstay bases. The mesh division was as follows:

- The backstay was meshed to a seed size of 30 mm.
- The core and external constraint elements of the BRBs were meshed to a seed size of 2 mm.

4.2. Reinforcement stress and displacement

Following external FD-BRB retrofitting with backstays, Figure 13 shows the stress and displacement distributions in the reinforcement system. Stress concentrations persist at the frame joints and column bases (Figure 13.a), exhibiting a 38.57 % maximum reduction compared to the pre-retrofit conditions (Figure 8.a), with significantly improved uniformity. This confirms the FD-BRB system's efficacy in terms of seismic energy dissipation and structural response enhancement. The displacements (Figure 13.b) peak near the second-floor midcolumns, with secondary concentrations in the top loading story and first-floor slab regions. The other regions exhibit minimal displacements. The BRB constraint elements and backstays exhibit negligible movement, although minor compressive displacements occur at the brace-backstay interfaces. Compared to the pre-retrofit conditions (Figure 8.b), the system achieved a maximum displacement reduction of 91.72 % and improved distribution uniformity.

The stress cloud diagrams of the beams, columns, and joints are shown in Figure 14. Maximum stresses are concentrated at the column bases, while secondary stress concentrations occur at the joints and adjacent regions. The remaining beams and columns exhibit uniformly distributed lower-stress levels.

This hierarchical pattern mirrors the stress distributions observed in the pre-retrofit configuration (Figures 4 and 5), although with a reduced overall magnitude. Stress redistribution is facilitated by the retrofit system, demonstrating enhanced

seismic performance through modified load-transfer mechanisms.

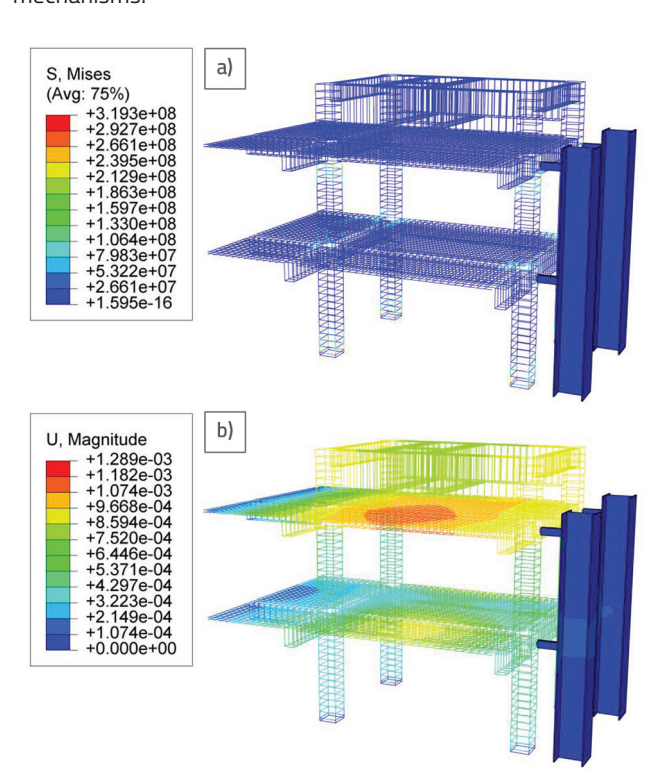


Figure 13. Reinforcement cloud diagrams of the frame after retrofitting: a) Stress; b) Displacement

The displacement distributions of the selected structural components are shown in Figure 15. First-floor joints JD1 and JD3 exhibit smaller displacements than second-floor joints JD5 and JD7. This displacement hierarchy is attributed to (1) the proximity of the vertical loading to the second-floor frame and (2) the higher horizontal loading magnitudes at the second-floor level.

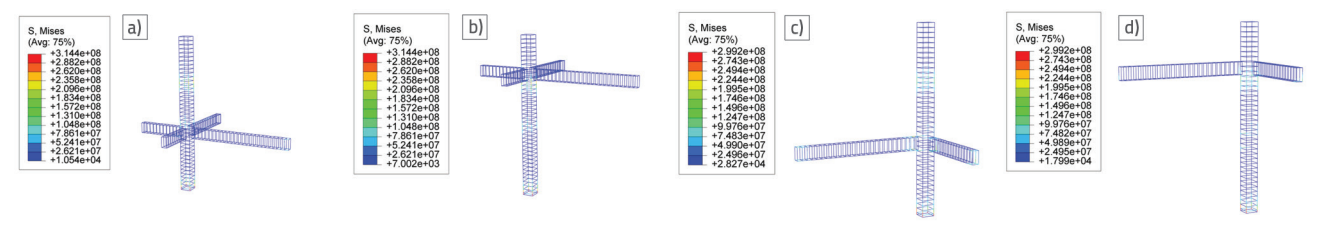


Figure 14. Stress cloud diagrams of the reinforcement in the beam-column joint: a) Z-1 and associated components; b) Z-5 and associated components; c) Z-3 and associated components; d) Z-7 and associated components

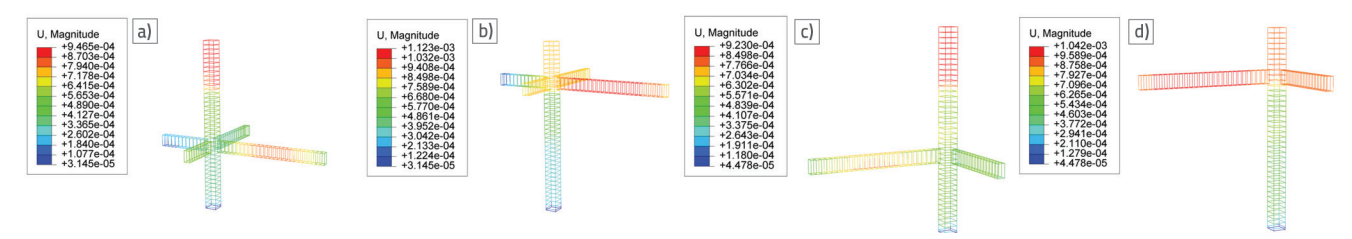


Figure 15. Displacement cloud diagrams of the reinforcement in the beam-column joint: a) Z-1 and associated components; b) Z-5 and associated components; c) Z-3 and associated components;

For the second-floor joints, positional variations result in differential displacements, with the maximum values occurring at corner-column joint JD7, followed by mid-column joint JD5, and the minimum values at the side-column joints. Within the vertical planes, the second-floor beam displacements exceed those of the first-floor beams corresponding to the vertical load distribution patterns.

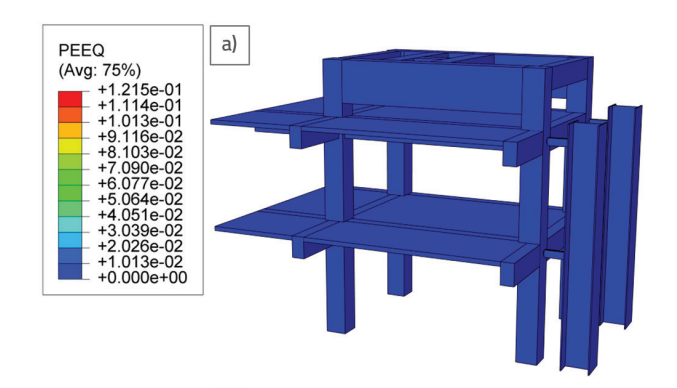
Compared with the pre-retrofit conditions (Figures 4 and 5), displacement reduction is achieved throughout the structure. Under low-cycle reciprocating loading, the external bracing system alters the structural response mechanisms, with energy dissipation primarily occurring within the supplemental damping system rather than in the primary frame. This energy redistribution provides structural protection by limiting the inelastic deformation in critical components.

4.3. Equivalent plastic strain and displacement of concrete

The equivalent plastic strain and displacement distributions of the retrofitted RCF structure are shown in Figure 16. The predominant blue colour in the equivalent plastic strain cloud diagram (Figure 16.a) indicates minimal concrete damage throughout the frame system. Compared to the pre-retrofit conditions (Figure 11.a), the plastic damage at the beam-column joints is substantially reduced under identical cyclic loading conditions. This damage mitigation demonstrates the enhanced structural performance of the FD-BRB retrofit system. The analysis results confirm that the plastic strain in the critical regions was significantly reduced, indicating effective structural protection under cyclic loading conditions.

An analysis of the displacement cloud diagram (Figure 16.b) reveals a substantial reduction in the overall displacement compared with the pre-retrofit conditions. Minimal displacement is observed at the column bases owing to the

constraint implementation. While the displacement pattern resembles the pre-retrofit distribution shown in Figure 11.b, a distinct difference can be noted: the post-retrofit displacements at the joints and adjacent components are distributed more uniformly.



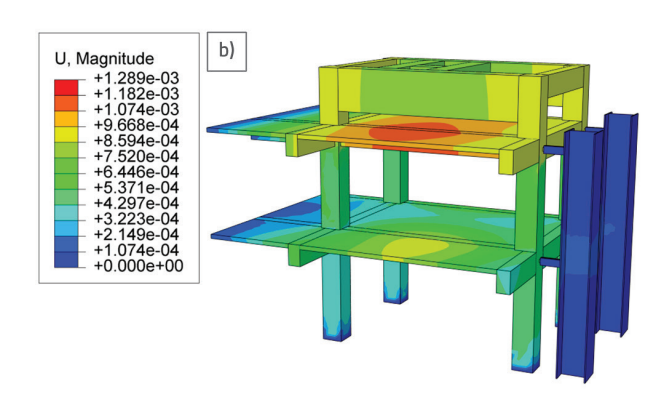


Figure 16. Concrete cloud diagrams of the frame after retrofitting: a) Equivalent plastic strain; b) Displacement

4.4. Performance analysis of the FD-BRB and backstay

The FD-BRB prototype was developed using a Mandelbrotderived geometric curve, and its 2D profile was drafted in AutoCAD and exported as a DXF file for import into ABAQUS. A three-dimensional solid model was subsequently established by employing C3D8R elements to accurately capture the complex stress states during tension-compression cycles. Material assignments were implemented as follows: external constraint elements utilised rectangular Q345 steel plates with a master surface designation on internal faces (E = 206GPa; v = 0.3), while core elements employed Q235 steel with a slave surface designation on external faces (E = 206GPa; v = 0.3). The backstays were modelled as H-section components (length: 4000 mm; cross-section: 400 × 400 mm; flange thickness: 15 mm; web thickness: 10 mm) using Q345 steel. Initial geometric imperfections equivalent to 0.1 % of the brace length were incorporated to account for fabrication tolerances.

The stress and displacement distributions within the FD-BRB core element are shown in Figure 17. An analysis of the stress cloud diagram reveals significant stress concentrations along the axial-loading direction. Elevated stresses are observed at the brace termination points and select fractal sawtooth features, although the yield thresholds remain not exceeded. The displacement field indicates maximum deformation near the frame connection interfaces, with progressive attenuation toward the backstay connections. This displacement gradient is attributed to accumulated damage at loading-initiation regions during low-cycle reciprocating loading. Consequently, enhanced connection reliability is recommended for experimental implementation and field applications to mitigate progressive deformation.

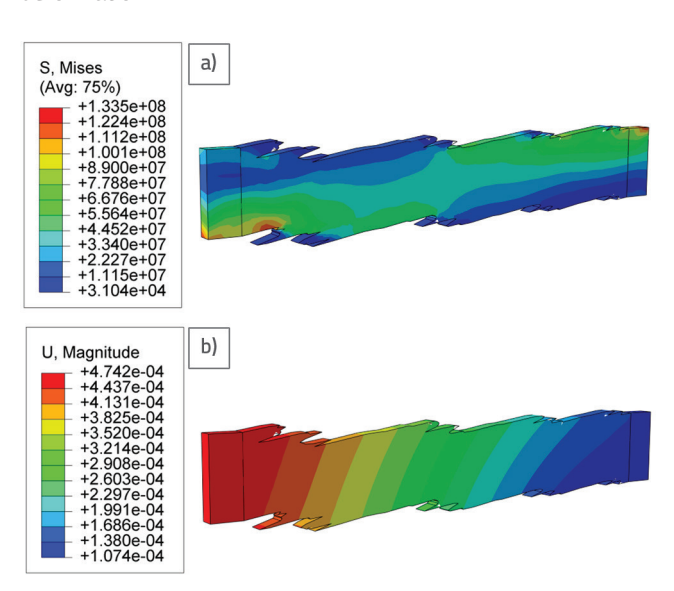


Figure 17. Cloud diagrams of the core element: a) Stress; b) Displacement

The stress and displacement distributions within the upper and lower external constraint elements are shown in Figure 18. Elevated stress concentrations are observed at the fractal serrations along the boundary interface, indicating a localised stress redistribution through geometric discontinuities. This stress dispersion mechanism enhances energy dissipation within the core element. Minimal stress is observed at the outermost constraint regions, confirming sufficient stiffness for effective core confinement. The displacement analysis reveals negligible deformation throughout the constraint elements, validating both the material selection and fractal boundary design compliance with structural specifications.

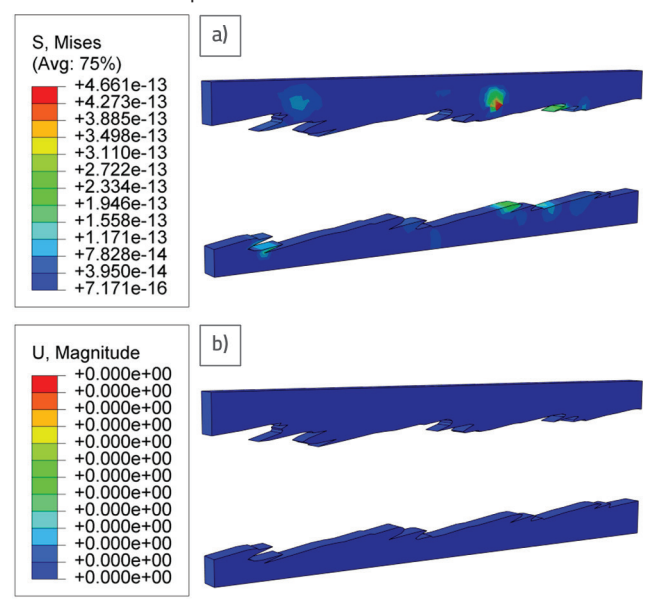


Figure 18. Cloud diagrams of the FD-BRB upper and lower external restraint elements: a) Stress; b) Displacement

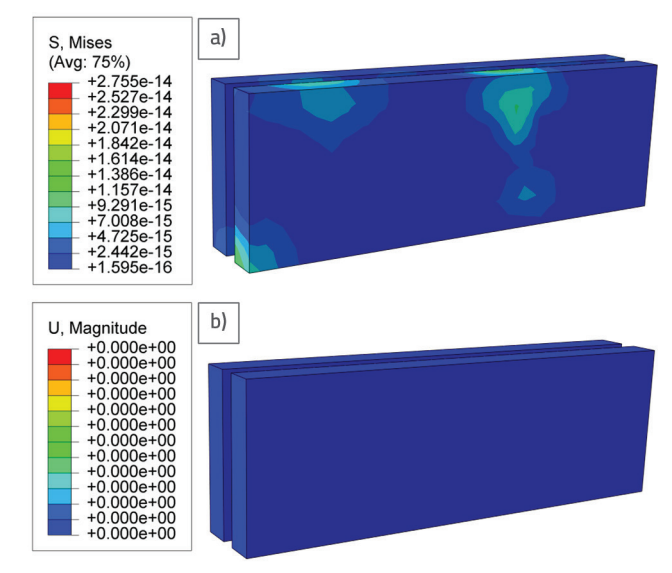


Figure 19. Cloud diagrams of the FD-BRB left and right external restraint elements: a) Stress; b) Displacement

The stress and displacement distributions in the lateral external restraint elements are shown in Figure 19. Significant stress concentrations are observed in the near-symmetrical regions of both steel plates (Figure 19.a), particularly adjacent to the severely weakened sawtooth boundaries. This stress pattern indicates localised frictional slip mechanisms at the core-constraint interface. Owing to the intentionally weak-axis destabilisation design of the core element, differential thickness configurations were implemented: the lateral plates exceeded the thickness of the upper and lower restraint plates. Consequently, substantially lower stress magnitudes are observed in the strong-axis direction compared to the observations in Figure 19.a. A displacement analysis (Figure 19.b) reveals negligible deformation throughout all restraint elements, validating compliance with strength and stiffness design specifications.

The stress and displacement distributions in the FD-BRB-connected backstays are shown in Figure 20. Elevated stress concentrations are observed at the brace connection interfaces (Figure 20.a), although the magnitudes remain below the yield thresholds. This confirms adequate stiffness and meets the design requirements. Secondary stress intensification occurs at fixed-base connections due to cyclic drift deformations, albeit at reduced magnitudes compared to the brace connection interfaces. Therefore, enhanced connection reliability is recommended for the base connection interfaces in experimental and field implementations.

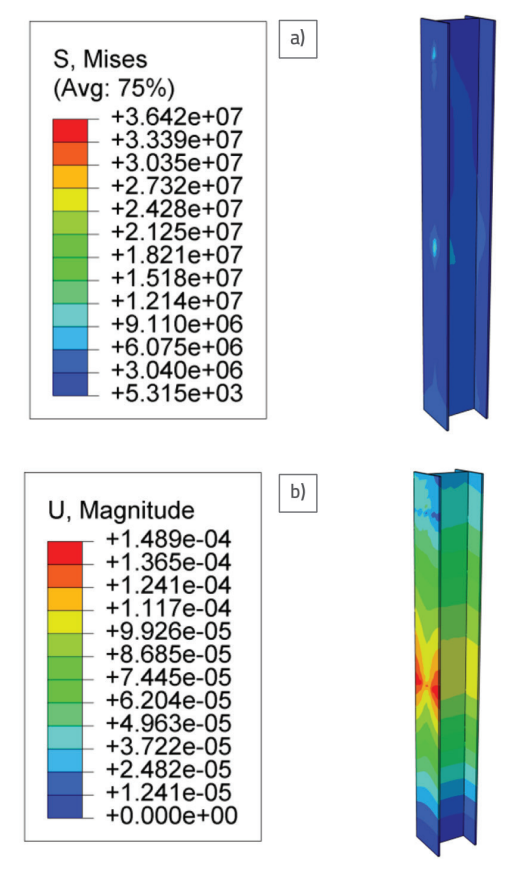


Figure 20. Backstay cloud diagrams: a) Stress; b) Displacement

A displacement analysis (Figure 20.b) reveals maximum deformation at the first-floor brace and backstay connection, with progressive attenuation toward both ends. This displacement gradient indicates cumulative deformation effects at the connections. Minimal displacement is observed at the constrained backstay bases, confirming effective boundary condition implementation. Consequently, a robust connection design is necessary at the brace end to mitigate external influence on structural performance.

5. Results before and after retrofitting

5.1. Numerical simulation results before and after retrofitting

Finite element analysis was used to compare the story drifts of the RCF structure under pre- and post-retrofit conditions (Figure 21). Maximum displacements at the first and second floors decreased from 7.1 and 16.9 mm (pre-retrofit) to 3.5 and 9.2 mm, respectively, following FD-BRB installation, representing a reductions of 50.7 % and 45.6 %, respectively. This significant displacement reduction demonstrates that the FD-BRB and backstay system simultaneously enhance the structural stiffness and dissipate seismic energy.

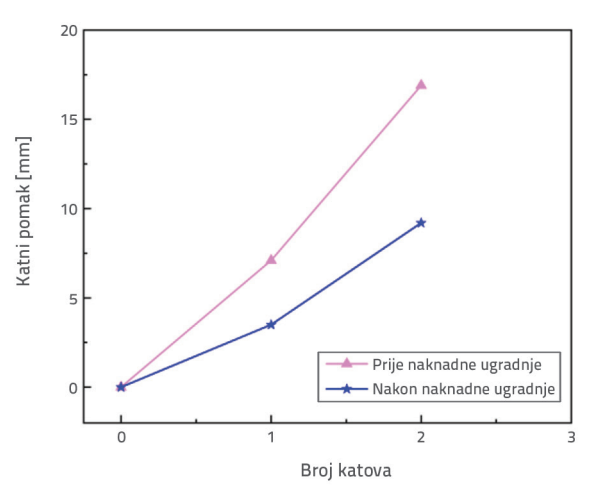
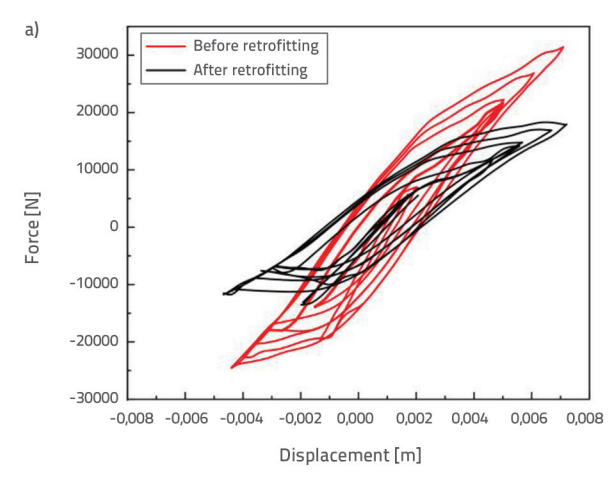


Figure 21. Story drift before and after retrofitting

The hysteresis curves for the first and second floors (Figure 22) were analysed to evaluate the energy dissipation performance before and after retrofitting. The pre-retrofit frame exhibits an initial stiffness lower than that of the strengthened system (Figure 22.a). Progressive loading causes significant stiffness degradation in the original structure and reduces its energy-dissipation capacity.

Following FD-BRB installation, the initial loading stages exhibit hysteresis behaviour comparable to that of the preretrofit system, confirming that the braces primarily provide supplemental stiffness without energy dissipation. During the



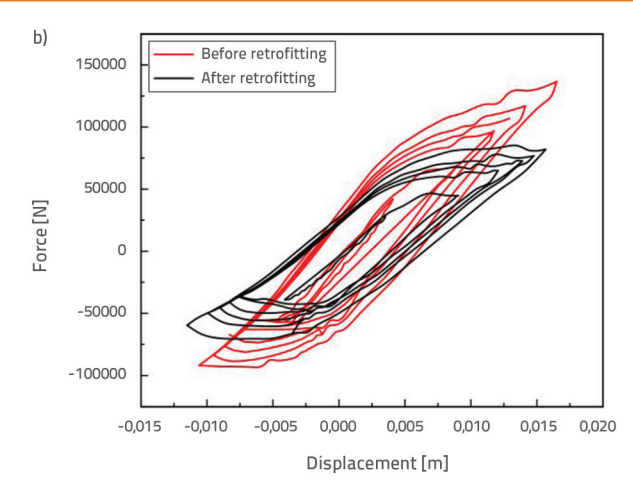


Figure 22. Hysteresis curves before and after retrofitting: a) First-floor; b) Second-floor





Figure 23. Field test photographs: a) Data acquisition; b) FD-BRB installation

mid-loading phases, the retrofitted system exhibits greater stiffness and fuller hysteresis loops, revealing simultaneous energy dissipation and stiffness enhancement. In the later loading stages, a gradual stiffness reduction and fusiform hysteresis loops emerge, demonstrating sustained energy dissipation under cyclic conditions. This confirms that the FD-BRB system enhances the structural resistance and mitigates degradation of the original frame.

The second-floor hysteresis patterns (Figure 22.b) mirror the first-floor behaviour with consistent loop shapes, albeit with differing magnitudes. This consistency between storeys validates the maintained composite action and substantially enhances the energy-dissipation performance throughout the retrofitted structure.

5.2. Comparison between the experimental results before and after retrofitting

Given length limitations, the experimental procedures are summarised rather than given in detail. The key test results and field photographs are presented in Figure 23. A comparative story drift analysis (Figure 24) reveals maximum pre-retrofit displacements of 7.7 and 17.7 mm on the first and second floors, respectively. Post-retrofit measurements decreased to 7.0 and 16.4 mm, respectively, representing reductions of 9.1 % and 7.3 %. This quantifiable displacement reduction demonstrates enhanced seismic performance via FD-BRB external reinforcement.

The hysteresis curves for the first and second floors of the RCF structure are shown in Figure 25. For the first floor (Figure 25.a), the pre-retrofit specimen exhibited maximum tensile and compressive displacements of 7.7 and 4.7 mm, respectively, at a 45-kN load. The retrofitted frame demonstrated significantly improved hysteresis behaviour under identical loading, with displacements of 7.0 (tension) and 3.9 mm (compression), confirming enhanced energy-dissipation capacity.

The second-floor responses (Figure 25.b) exhibit a similar behaviour. The pre-retrofit hysteresis loops remained small and bow-shaped during the elastic stages and transitioned into enlarged loops with progressive yielding under increased loading. Cycling effects reduce the horizontal stiffness through pinching phenomena, thereby decreasing the energy dissipation.

At a 225-kN load, the pre-retrofit tensile and compressive displacements were 17.7 and 14.5 mm, respectively. Post-retrofit displacements decreased to 16.4 (tension) and 11.9 mm (compression), demonstrating both displacement reduction and increased load-carrying capacity.

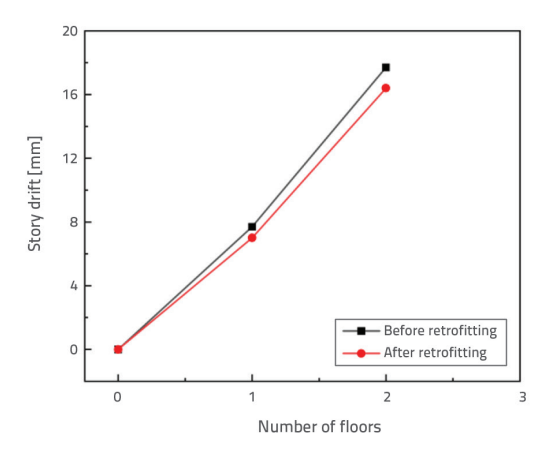
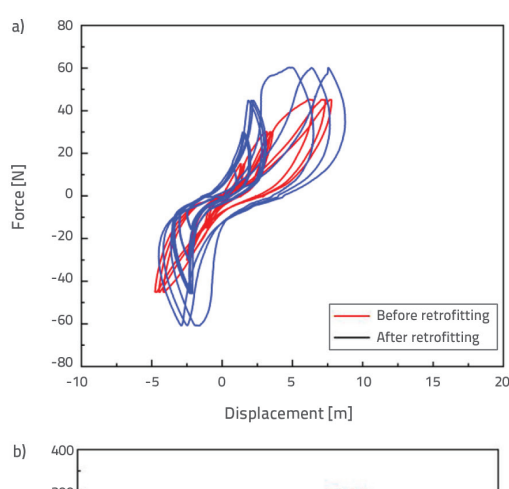


Figure 24. Story drift comparison



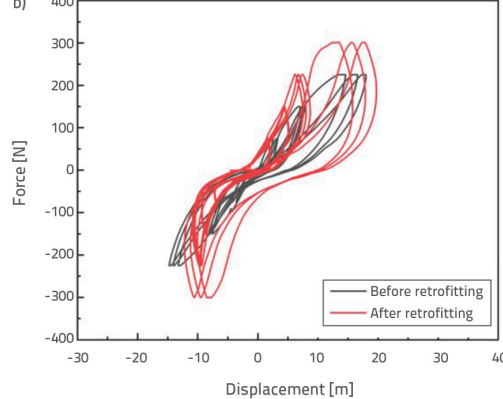


Figure 25. Hysteresis curves before and after RCF retrofitting: a) First and b) second floors

The energy-dissipation performance of the FD-BRB-retrofitted RCF system was experimentally analysed (Figure 26). The FD-BRB initially operated within the linear elastic range, and its energy-dissipation proportion increased progressively with displacement

amplitude. At a 4-mm displacement, the braces contributed to 50 % of the total system energy dissipation. At a 10-mm displacement, the base RCF structure's dissipation capacity stabilised, whereas at a 15-mm displacement, the FD-BRBs accounted for 70.8 % of the total energy dissipation. This demonstrates that the FD-BRBs function as the primary protective mechanism, assuming a dominant energy-dissipation role during severe seismic demands.

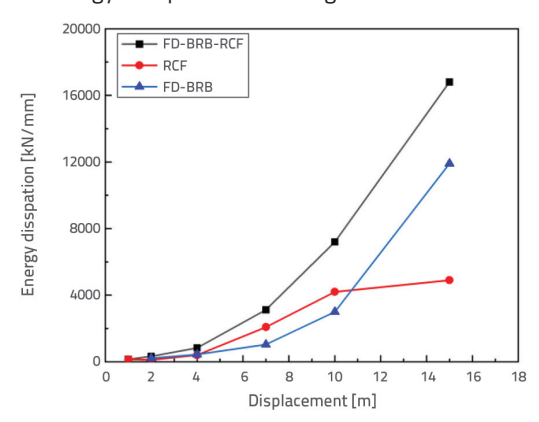


Figure 26. Energy-dissipation-displacement relationship

6. Conclusion

Following FD-BRB retrofitting, the structural components (beams, columns, and joints) achieved improved stress distribution uniformity with a maximum stress reduction of 38.57 %. This significant stress mitigation confirmed the capacity of the FD-BRB system to enhance energy dissipation. Concurrently, the displacements decreased by up to 91.72 % compared to the non-retrofitted structure, demonstrating exceptional deformation control.

The retrofitted system exhibited a substantially enhanced hysteresis behaviour, as manifested by fuller hysteresis loops. This improvement simultaneously increased the lateral load-bearing capacity by 28 % and maintained the maximum story drift angles below the $\theta < 1/50$ threshold. The modified load-transfer pathways observed in the system provide critical data for advancing computational mechanics models of externally reinforced RC frames.

Discrepancies between the simulation and experimental results were observed. These differences are primarily attributed to the necessary simplifications adopted in the numerical modelling, particularly the implementation of idealised constitutive relationships and boundary conditions, which streamline complex physical processes while mitigating confounding factors such as environmental variability or measurement artifacts. Consequently, finite element analysis should be employed as a complementary methodology alongside physical testing and comparative validation to enhance the structural assessment reliability.

Acknowledgement

This paper was supported by the Science and Technology Plan Project of Qinghai Province (No. 2024-ZJ-975).

REFERENCES

- [1] Sarno, L., Manfredi, G.: Experimental tests on full-scale RC unretrofitted frame and retrofitted with buckling-restrained braces, Earthquake Engineering & Structural Dynamics, 41 (2012) 2, pp. 315–333, https://doi.org/10.1002/eqe.1131
- [2] Abou-Elfath, H., Ramadan, M., Alkanai, F.: Upgrading the seismic capacity of existing RC buildings using buckling restrained braces, Alexandria Engineering Journal, 56 (2017) 2, pp. 251-262, https://doi.org/10.1016/j.aej.2016.11.018
- [3] Mirtaheri, M., Sehat, S., Nazeryan, M.: Improving the behavior of buckling restrained braces through obtaining optimum steel core length, Structural Engineering and Mechanics, 65 (2018) 4, pp. 401-408, https://doi.org/10.12989/sem.2018.65.4.401
- [4] Mirtaheri, M., Gheidi, A., Zandi, A., et al.: Experimental optimization studies on steel core lengths in buckling restrained braces, Journal of constructional steel research, 67 (2011) 8, pp. 1244-1253, https://doi.org/10.1016/j.jcsr.2011.03.004
- [5] Bai, J., Cheng, F., Jin, S., et al.: Assessing and quantifying the earthquake response of reinforced concrete buckling-restrained brace frame structures, Bulletin of Earthquake Engineering, 17 (2019), pp. 3847– 3871, https://doi.org/10.1007/s10518-019-00633-0
- [6] Li, G., Li, J., Fang, C., et al.: Seismic performance of two-story three-bay reinforced concrete frame equipped with K-configured buckling restrained braces, Journal of Building Engineering, 74 (2023), 106904, https://doi.org/10.1016/j.jobe.2023.106904
- [7] Mebarek, K., Bourahla, N., Remki, M.: Performance evaluation of masonry Infilled RC frame structures under lateral loads, GRAĐEVINAR, 73 (2021) 3, pp. 219-234, https://doi. org/10.14256/JCE.2647.2019
- [8] Valarmathi Moorthy, G., Thangaraj, P., Gobi Shanmugam, T.: Structural behavior of a single bay two-story basalt fiber reinforced concrete frame, GRAĐEVINAR, 74 (2022) 12, pp. 1085-1092, https://doi.org/10.14256/JCE.3550.2022
- [9] Koman, H., Nohutcu, H., Kılıç, G., et al.: Poboljšanje ponašanja AB okvira s blokovima bez morta pri potresu, GRAĐEVINAR, 77 (2025) 3, pp. 219-236, https://doi.org/10.14256/JCE.3920.2023
- [10] Kallioras, S., Bournas, D., Koutas, L., et al.: Integrated seismic and energy retrofitting of masonry-infilled RC buildings with textilereinforced mortar and thermal insulation: Full-scale tests on a five-story prototype, Journal of Building Engineering, 98 (2024), 111006, https://doi.org/10.1016/j.jobe.2024.111006
- [11] Yooprasertchai, E., Warnitchai, P.: Seismic retrofitting of low-rise nonductile reinforced concrete buildings by buckling-restrained braces, Proceedings of 14th World Conference on Earthquake Engineering, Beijing, 2008.
- [12] Dinu, F., Bordea, S., Dubina, D.: Strengthening of non-seismic reinforced concrete frames of buckling restrained steel braces, Behaviour of steel structures in seismic areas, eds. F. Mazzolani, R. Herrera, London, pp. 1085-1090, 2012.
- [13] Mahrenholtz, C., Lin, P., Wu, A., et al.: Retrofit of reinforced concrete frames with buckling-restrained braces, Earthquake Engineering & Structural Dynamics, 44 (2015) 1, pp. 59-78, https://doi.org/10.1002/eqe.2458
- [14] Ozcelik, R., Erdil, E.: Pseudodynamic test of a deficient RC frame strengthened with buckling restrained braces, Earthquake Spectra, 35 (2019) 3, pp. 1163-1187, https://doi.org/10.1193/122317EQS263M
- [15] Tsai, K., Hsiao, P., Wang, K., et al.: Pseudo-dynamic tests of a full-scale CFT/BRB frame—Part I: Specimen design, experiment and analysis, Earthquake Engineering & Structural Dynamics, 37 (2008) 7, pp. 1081-1098, https://doi.org/10.1002/eqe.804

- [16] Corte, G., D'Aniello, M., Landolfo, R.: Field testing of all-steel buckling-restrained braces applied to a damaged reinforced concrete building, Journal of structural engineering, 141 (2015) 1, D4014004, https://doi.org/10.1061/(ASCE)ST.1943-541X.0001080
- [17] Islam, S., Huang, S., Skokan, M., et al.: Performance based seismic retrofit of a high-rise tower using buckling restrained braced frames, 8th US National conference on earthquake engineering, San Francisco, California, USA, 2006.
- [18] Cao, X., Feng, D., Wu, G.: Seismic performance upgrade of RC frame buildings using precast bolt-connected steel-plate reinforced concrete frame-braces, Engineering Structures, 195 (2019), pp. 382-399, https://doi.org/10.1016/j.engstruct.2019.06.007
- [19] Cao, X., Feng, D., Wu, G.: Pushover-based probabilistic seismic capacity assessment of RCFs retrofitted with PBSPC BRBF substructures, Engineering Structures, 234 (2021), 111919, https:// doi.org/10.1016/j.engstruct.2021.111919
- [20] Sutcu, F., Bal, A., Fujishita, K., et al.: Experimental and analytical studies of sub-standard RC frames retrofitted with bucklingrestrained braces and steel frames, Bulletin of Earthquake Engineering, 18 (2020), pp. 2389-2410, https://doi.org/10.1007/ s10518-020-00785-4
- [21] Bergami, A.: Design of Additional Dissipative Structures for Seismic Retrofitting of Existing Buildings, Applied Sciences, 14 (2024) 6, 2477, https://doi.org/10.3390/app14062477
- [22] Olivo, J., Cucuzza, R., Bertagnoli, G., et al.: Optimal design of steel exoskeleton for the retrofitting of RC buildings via genetic algorithm, Computers & Structures, 299 (2024), 107396, https:// doi.org/10.1016/j.compstruc.2024.107396
- [23] Luo, X., Song, Y., Wang, T., et al.: Parameter design and mechanical performance of a new type of fractal buckling restrained brace, Journal of Jilin University, 52 (2022) 7, pp. 1607–1619 (in Chinese), https://doi.org/10.13229/j.cnki.jdxbgxb20210031
- [24] Jin, Z.: Study on seismic performance of external F-D bucklingrestrained brace, Lanzhou University of Technology (in Chinese), https://doi.org/10.27206/d.cnki.ggsgu.2020.001457, 2020.
- [25] Ma, L., Luo, X., Ren, Y.: Design and performance study of diamond-shaped opening structure of fractal buckling restrained brace core unit, Journal of Qinghai University, 42 (2024) 5, pp. 78-85 (in Chinese), https://doi.org/10.13901/j.cnki.qhwxxbzk.2024.05.011
- [26] Ren, Y., Ma, L., Luo, X.: Study on the performance of different parameters of fractal dimension- buckling restrained brace based on core elements weakening, Building Science, 40 (2024) 11, pp. 101-112 (in Chinese), https://doi.org/10.13614/j.cnki.11-1962/tu.2024.11.013
- [27] GB50010-2021, Code for design of concrete structures, China Architecture & Building Press, 2014. (in Chinese)
- [28] Wang, Y., Song, H.: Working mechanism study on bucklingrestrained brace in displacement mode, Journal of Henan Polytechnic University, 32 (2013) 5, pp. 631-638 (in Chinese), https://doi.org/10.16186/j.cnki.1673-9787.2013.05.014
- [29] Wang, Y.: Research on seismic performance and design method of buckling-restrained brace and brace-frame structure, China University of Mining and Technology (in Chinese), 2014.
- [30] Kou, H.: Research on influence of high-rise concrete frame shear structure characteristics with BRB seismic reduction and reinforcement, Lanzhou University of Technology (in Chinese), https://doi.org/10.27206/d.cnki.ggsgu.2020.000891, 2020.
- [31] Wu, C.: Study on seismic behavior of a new type of replaceable energy-consuming coupling beam, Hebei University of Engineering (in Chinese), https://doi.org/10.27104/d.cnki.ghbjy.2020.000281, 2020.